Nanoscale

Accepted Manuscript

This article can be cited before page numbers have been issued, to do this please use: Y. Fan, S. Li, Y. Wang, C. Zhuang, X. Liu, Z. Guangshan and X. Zou, *Nanoscale*, 2020, DOI: 10.1039/D0NR04098C.

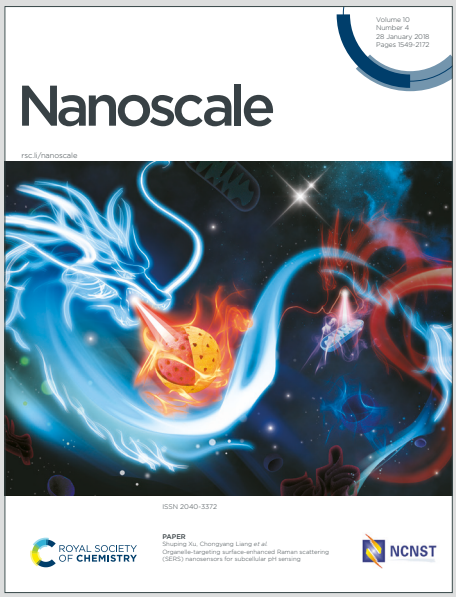

ROYAL SOCIETY OF CHEMISTRY

rsc.li/nanoscale

View Article Online
DOI: 10.1039/D0NR04098C

ARTICLE

Tuning the synthesis of polymetallic-doped ZIFs derived materials for efficient hydrogenation of furfural to furfuryl alcohol

Received 00th January 20xx,
Accepted 00th January 20xx

DOI: 10.1039/x0xx00000x

Yafei Fan,[a] Shangjing Li,[a] Ying Wang,[a] Changfu Zhuang,*[a] Xiaoteng Liu,[c] Guangshan Zhu[b] and Xiaoqin Zou*[b]

Cu, Co and Zn modified N-doped porous carbons (CuCo/Zn@NPC) are prepared using a polymetallic homogeneous doping and self-templating method as high performance non-noble metal catalysts for the hydrogenation of furfural (FF) to furfuryl alcohol (FAL). The CuCo/Zn@NPC-600 catalyst after treated at 600 °C shows a superior catalytic activity with nearly 100% conversion of FF and an almost 100% selectivity of FAL using H_2 at 140 °C. Meanwhile in the catalytic transfer hydrogenation (CTH) using 2-propanol as H-donor, the conversion of FF reaches 95.8% and the selectivity of FAL is 99.1%. The results show that the Zn dopant leads to 37.3 times higher yield on CuCo/Zn@NPC-600 catalyst than that on CuCo@NPC-600, and 2.3 times higher than that of Co/Zn@NPC-600 with Cu dopant. The efficient activity of the CuCo/Zn@NPC-600 catalyst is mainly due to the highly dispersed metal nanoparticles, the advanced porous structure resulted from Zn escape from the precursor template, and the synergistic effect between Cu and Co. Furthermore, the CuCo/Zn@NPC-600 catalyst exhibits good recyclability of FF hydrogenation in four cycle tests. The advanced synthesis of using homogeneous doping and self-template strategy sheds light on preparing effective catalysts for hydrogenation of biomass-based compounds.

1. Introduction

Increasing attention has been paid on the research of the conversion of biomass-derived compounds into value-added chemicals using non-noble metal catalysts.[1-3] Furfural (FF), can be obtained from hemicelluloses via acid-catalyzed hydrolysis and dehydration, serves as an important platform compound for biofuels production and chemicals.[4-7] The C=C and C=O bonds on FF are easily hydrogenated and more than 80 compounds can be directly or indirectly yielded.[8] Different catalysts can tune the selectivity of FF hydrogenation to produce furfuryl alcohol (FAL),[9] tetrahydrofurfuryl alcohol (THFA),[10] 2-methylfuran (2-MF),[11] furan (THF),[12] cyclopentanone,[13] cyclopentanol[14] and levulinic acid.[15] Among them, FAL is a versatile intermediate to produce adhesives, resins and synthetic fibers.[16] However, it still is a challenge to control the FAL selectivity in FF hydrogenation because this reaction pathway is very complex, which largely relies on catalysts.[17]

So far, industrialized FF to FAL hydrogenation has been successfully processed through using copper chromite catalyst.[18] Due to the harsh reaction conditions and high toxicity of chromium trioxide, a variety of chromium-free catalysts, especially Pd,[19] Pt,[20] Ru,[21] Ni[22] and Cu,[23] have been extensively studied in liquid-phase hydrogenation of FF. However, C=C is also easy to be activated for hydrogenation in the process of FF hydrogenation. Therefore, it will be accompanied by the generation of THFA and 2-MF, and the selectivity of targeted product is generally low.[24-26] In order to make the metal catalysts show greater hydrogenation selectivity for C=O, the researchers adjusted the space structure and electronic state around the metal active center by introducing the second metal and the metal-support interaction.[27-28] Nevertheless, these approaches to improve selectivity may also cause a reduction to the catalytic activity. Therefore, it is urgent to develop non-noble metal catalysts with high activity and selectivity to regulate the competitive reactivity between C=O and C=C under mild conditions.

Porous carbon has been proven to be an excellent catalyst support, especially the hierarchical porous carbon materials can efficiently increase the transport of reactants/products and stabilize dispersed nanoparticles.[29] Compared with pure porous carbons, N-doped porous carbons (NPC) are better for supporting metals owing to better metal distribution, smaller

[a] Key Laboratory of Forest Resources Conservation and Utilization in the Southwest Mountains of China, Ministry of Education, Southwest Forestry University, Kunming 650051, P. R. China. E-mail: cfzhuang@swfu.edu.cn (Changfu Zhuang)
[b] Faculty of Chemistry, Northeast Normal University, Changchun 130024, P. R. China. E-mail: zouxq100@nenu.edu.cn (Xiaoqin Zou)
[c] Department of Mechanical and Construction Engineering, Faculty of Engineering and Environment, Northumbria University, Newcastle upon Tyne, NE1 8ST, UK.
† Electronic Supplementary Information (ESI) available: See DOI: 10.1039/x0xx00000x

DOI: 10.1039/D0NR04099C

metal size and enhanced electron interactions in supported metal catalysts (M@NPC), making M@NPC extremely advantageous in catalytic hydrogenation.[30-31] Due to their extremely high specific surface area, adjustable channel size and regulated polymetallic coordination, zeolitic imidazolate frameworks (ZIFs) materials have become excellent precursors for M@NPC.[32] As the precursor, ZIF-8 has been proven to provide hierarchical porosity with high nitrogen content because of the evaporation of Zn, however, it can't afford critical catalytic sites for metals such as Co.[33] Co-based ZIF-67, isostructural to ZIF-8, has metal active site Co, but the surface area and porosity are low after precursor carbonization.[34] M@NPC derived from bimetallic ZIFs (BMZIFS) based on Co and Zn reserving both advantages independently from ZIF-8 and ZIF-67, has outstanding porous structure and dispersed Co active sites.[35-36] However, these mono-metallic and bi-metallic catalysts still can't meet the requirements of adjustable catalytic performance at high activity and selectivity. Therefore, the synthesis of catalyst with high activity and selectivity by a simple method is of great significance for hydrogenation of FF.

We speculate that the introduction of other metals into the BMZIFS, especially the third metal to partially replace Zn or Co, may introduce more metal active centers and endow BMZIFS derivatives more unique catalytic properties. Copper (Cu) is chosen as the third metal because it can more selectively hydrogenate the C=O bond rather than the C=C bond. Previous studies have confirmed that FAL is mainly absorbed vertically on the Cu surface, that is, the O atom on the C=O is bound to the Cu surface.[37-38] Therefore, Cu doped BMZIFS (Cu-BMZIFS) as self-sacrificial precursors, using nitrogen-doped porous carbon (NPC) as the support and regulating the composition of catalysts, could achieve the expected effect of high activity and selectivity in the catalytic hydrogenation from FF to FAL.

In this work, the N-doped porous carbon supported Cu, Co and Zn catalysts (CuCo/Zn@NPC) are prepared by the method of homogeneous doping and self-templating for selective hydrogenation of FF to FAL. The catalytic properties of CuCo/Zn@NPC catalysts are investigated in detail by a series of characterizations and controlled experiments. The CuCo/Zn@NPC-600 catalyst shows the optimal catalytic activity and selectivity, superior to other catalysts doped with different metals. The catalyst also has a good performance when used for liquid-phase catalytic transfer hydrogenation (CTH) of FAL using 2-propanol as H-donor. In addition, recycling experiments show that CuCo/Zn@NPC-600 has remarkable stability.

2. Experimental

2.1 Materials

$Cu(NO_3)_2{\cdot}6H_2O$, $Co(NO_3)_2{\cdot}6H_2O$ and $Zn(NO_3)_2{\cdot}6H_2O$ were purchased from Adamas Reagent Co., Ltd. Dimethylimidazole was obtained from TCI (Shanghai) Development Co., Ltd. Furfural, furfuryl alcohol, tetrahydrofuran, 2-propanol, methyl alcohol, ethyl alcohol, acetonitrile, methylbenzene and 1,4-dioxane were purchased from Sinopharm Chemical Reagent Co., Ltd. In addition, the commercial noble metals catalysts were purchased from Aladdin Reagent. All chemicals were used without further treatments.

2.2 Synthesis of Cu-BMZIFS

$Cu(NO_3)_2{\cdot}6H_2O$ (3 mmol), $Co(NO_3)_2{\cdot}6H_2O$ (9 mmol), $Zn(NO_3)_2{\cdot}6H_2O$ (3 mmol) and 80 mL of methanol were firstly mixed in a flask using magnetic stirrer. Dimethylimidazole (96 mmol) was dissolved in 120 mL of methanol and then added into the mixture followed by stirring at room temperature for 24 hours. The product was separated by centrifugal method and washed subsequently with methanol for three times and dried at 80 °C under vacuum for overnight. Other ZIFs were synthesized by the same method as Cu-BMZIFS. The Cu-ZIF-67 has Cu and Co, Cu-ZIF-8 has Cu and Zn, BMZIFS has Co and Zn, ZIF-67 and ZIF-8 have single Co and single Zn, respectively.

2.2 Synthesis of CuCo/Zn@NPC-T

Cu-BMZIFS were firstly heated at 200 °C in a tube furnace under argon environment for 1 h, then treated at various elevated temperatures (T=500, 600, 700, 800, 900 °C) with a heating ramp of 5 °C min^{-1} and kept at that temperature for 4 h followed by natural cooling to room temperature. The obtained material was named CuCo/Zn@NPC-T according to the temperature and it was used for the hydrogenation of FF without further treatment. Cu-ZIF-67, Cu-ZIF-8, Cu-ZIF, ZIF-67 and ZIF-8 were named CuCo@NPC-T, Cu/Zn@NPC-T, Cu@NPC-T, Co@NPC-T and Zn@NPC-T through the same pyrolysis process as that of Cu-BMZIFS, respectively. For a detailed synthesis of impregnation-CuCo/Zn@NPC and adsorption-CuCo/Zn@NPC, see supporting information.

2.3 Characterization

Powder X-ray diffraction (XRD) patterns were analyzed using a Rigaku Ultima X-ray diffraction spectrometer with Cu Kα radiation (λ = 1.5418 Å) at 40 kV and 40 mA. Brunauer-Emmet-Teller (BET) specific area and pore size distribution of the catalysts were obtained using N_2 adsorption-desorption measurement at 77 K using ASAP 2020 Plus Physisorption instrument. XPS analysis was performed on a PHI5000 Versa probe-II Scanning XPS Microprobe system. The morphology of the catalyst was inspected using a scanning electron microscope (SEM, Hitachi SU8010) equipped with an energy dispersive X-ray spectrometer (EDS) and a high-resolution transmission electron microscope (HR-TEM, JEM-2100). The mental contents in the samples were measured by ICP-OES using a VISTA-MPX instrument.

2.4 Catalysis measurement

Typically, the hydrogenation of FF was performed in a 25 mL autoclave reactor with a reaction solution of 2.5 mmol FF, 25 mg catalyst and 8 mL tetrahydrofuran. The reactor was first purged three times with H_2 and then pressurized to 2 MPa. The reactor was then heated to 140 °C for 4 h with a stirring rate of 800 rpm. After reaction, the liquid samples were collected using a filter membrane for further test and the used catalyst was filtered, washed with ethanol and then dried at 80

°C in vacuum. Then the catalyst was treated at 600 °C for further reactions and characterizations.

The liquid products were distinguished by gas chromatography-mass spectrometry (GCMS-QP2010 SE, Shimadzu) and was quantitatively analyzed by GC (GC-7890A, Agilent), equipped with FID detector and a (30 m × 0.25 mm × 0.25 μm) KB-WAX capillary column (Kromat Corporation, USA). In addition, the liquid products were diluted in methanol before the analysis. 1.0 uL sample was injected into the injection port with a split ratio of 30:1. The column temperature was initially maintained at 40 °C for 1 min followed by heating up to 220 °C at a ramp rate of 20 °C min^{-1} and the temperature was held at 250 °C using nitrogen as the carrier gas.

The conversion of reactant is defined with the following equation:

$$\text{Conversion (\%)} = \frac{\text{Mole of reactant converted}}{\text{Mole of reactant loaded}} \times 100\%$$

The selectivity of product is defined with the following equation:

$$\text{Selectivity (\%)} = \frac{\text{Mole of furfuryl alcohol produced}}{\text{Mole of product produced}} \times 100\%$$

3. Results and discussion

3.1. Characterization of catalysts

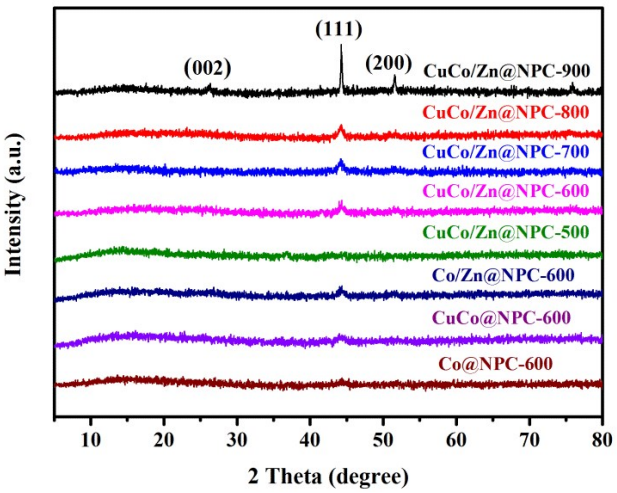

Fig. 1 XRD patterns of the M@NPC-600 and CuCo/Zn@NPC-T materials.

Fig. S1 is the XRD patterns of a series of ZIF-8, ZIF-67 and BMZIFS, and all ZIFs samples show same XRD peak profile, which indicates their same crystal structure. The XRD patterns of M@NPC-600 and CuCo/Zn@NPC-T samples are shown in Fig. 1. The ordered crystal structure of ZIFs completely collapses after calcination. Three diffraction peaks at near 44.2°, 51.6° and 76.0° are ascribed to (111), (200) and (220) planes of face-centered-cubic (fcc) Co (JCPDS No. 15-0806). With calcination temperature increased from 500 to 900 °C, the peak width becomes narrower and peak intensity gets stronger. The result suggests an increased crystallinity and size of metal nanoparticles in CuCo/Zn@NPC-T materials with the pyrolysis temperature increased, consistent with the size distributions from TEM analysis (Fig. S2). The peak located around 25° is originated from a carbon (002) diffraction of typical graphite carbon (JCPDS No. 08-0415). The graphitization degree of carbon in M@NPC-600 and CuCo/Zn@NPC-T is relatively low, shown by weak C (002) associated XRD peak. The graphite carbon is further analyzed in the following HR-TEM (Fig. 5). The characteristic peaks of Cu and Zn are undetectable because of either small particles or low contents, but their existences will be confirmed by EDS mapping (Fig. 3), ICP-OES (Table 1) and XPS spectrum (Fig. S3).

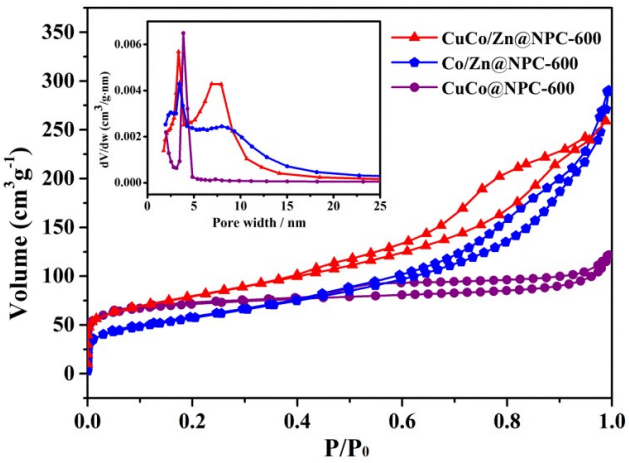

Fig. 2 Nitrogen adsorption-desorption isotherms of the M@NPC-600 materials (inset is the pore size distribution).

To analyze the porous nature of the samples, N_2 adsorption and desorption isotherms of CuCo/Zn@NPC-600, Co/Zn@NPC-600 and CuCo@NPC-600 are shown in Fig. 2, and CuCo/Zn@NPC-T materials in Fig. S4. The N_2 adsorption isotherm of CuCo/Zn@NPC-T has a sharp increase below P/P_0 = 0.02 and a hysteresis loop above P/P_0 = 0.5. Thus, the co-presence of micropores and mesopores is shown by the N_2 adsorption isotherm. Barrett-Joyner-Halenda (BJH) analyses show that the sample have two sets of mesopores. The first one is the pore size of 2-4 nm in CuCo/Zn@NPC-600, similar to 2.2 nm in Cu-BMZIFS (Table 1), indicating CuCo/Zn@NPC-600 still inherits some of the original pore size of Cu-BMZIFS. The other pore size distribution in CuCo/Zn@NPC-600 is located in the larger mesoporous range of 5-10 nm (Fig. 2) and the average pore size is about 6.7 nm (Table 1). But the pore size distribution in CuCo@NPC-600 shows that most of the pores fall into the narrow range of 3-4 nm, which is due to the lack of Zn volatilization. The presence of Zn, the only difference between CuCo/Zn@NPC-600 and CuCo@NPC-600, leads to a significant difference in their porous nature. As shown in Table 1, the surface area of 275 m^2 g^{-1} and pore volume of 0.36 cm^3 g^{-1} for CuCo/Zn@NPC-600 are much bigger than 206 m^2 g^{-1} and 0.11 cm^3 g^{-1} for CuCo@NPC-600. CuCo@NPC-600 also has a smaller specific surface area than Co/Zn@NPC-600 and Cu/Zn@NPC-600. This result demonstrates that the introduction of Zn can obviously improve the porosity of the pyrolytic material. CuCo/Zn@NPC-900 has a maximum pore

View Article Online DOI: 10.1039/D0NR04099C

size up to 7.8 nm and the pore volume reaches 0.52 $cm^3 g^{-1}$. This may be caused by almost all Zn elements of CuCo/Zn@NPC-900 are sublimated out during the pyrolysis process, evidenced by only 0.12% Zn content measured by ICP-OES (Table 1). This result shows that increasing the temperature can lead to larger pore size and higher pore volume in CuCo/Zn@NPC-T materials.

Table 1. The specific surface area, pore volume, pore size, metal particle size and metal content of the catalysts.

Sample	S_{BET} [a] ($m^2 g^{-1}$)	Pore volume [a] ($cm^3 g^{-1}$)	Pore size [a] (nm)	Metal particle size (nm)	Co [b] (wt%)	Cu [b] (wt%)	Zn [b] (wt%)
Cu-BMZIFS	1372	0.76	2.2	-	10.41	0.29	7.36
CuCo/Zn@NPC-500	226	0.36	5.7	9.5	13.75	0.38	6.88
CuCo/Zn@NPC-600	275	0.36	6.7	11.8	14.79	0.44	4.73
CuCo/Zn@NPC-700	315	0.47	5.8	13.2	15.45	0.46	1.94
CuCo/Zn@NPC-800	280	0.45	5.9	73.8	16.97	0.49	0.47
CuCo/Zn@NPC-900	239	0.52	7.8	137.8	17.54	0.52	0.12
Co/Zn@NPC-600	224	0.46	8.4	12.5	18.69	-	10.03
Cu/Zn@NPC-600	324	0.32	5.9	-	-	2.91	18.25
CuCo@NPC-600	206	0.11	6.1	16.9	15.83	0.63	-

[a]: by ASAP 2020 Plus, [b]: by ICP-OES.

SEM surface morphology of Cu-BMZIFS, CuCo/Zn@NPC-600 and its EDS mapping scan are shown in Fig. 3. It can be seen from Fig. 3a that the Cu-BMZIFS exhibits an ordinary dodecahedron shape. As shown in Fig. 3b, the CuCo/Zn@NPC-600 material almost maintains the shape but with rougher surface than the Cu-BMZIFS precursor. As compared with the crystal size of 600-700 nm for Cu-BMZIFS, the particle size of CuCo/Zn@NPC-600 is decreased to 300-400 nm due to volume shrinkage at high temperature. The EDS mapping of CuCo/Zn@NPC-600 (Fig. 3c) shows a straight-forward evidence for the existence of various elements C, N, Co, Zn and Cu. All the elements are evenly distributed amongst CuCo/Zn@NPC-600. Among them, the Cu signal is very weak because Cu content is only 0.44% by ICP-OES measurement, consistent with unable detection of Cu by XRD and HR-TEM. The actual doping amount of Cu is far less than the excess addition in the synthesis precursor, because Cu is rather more difficult for Cu than Zn or Co to form the ZIFs structure.[39-40]

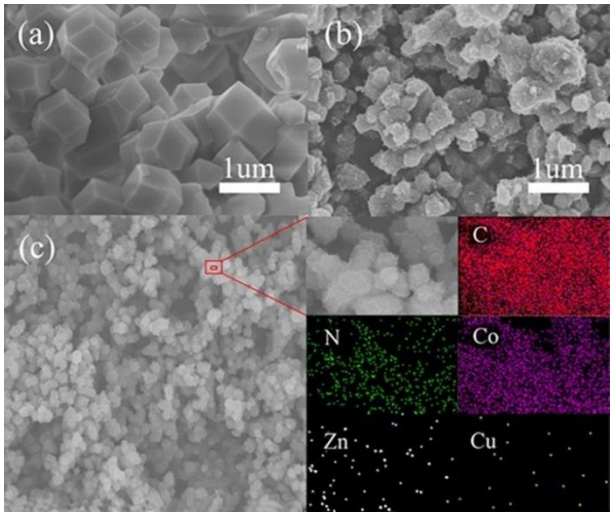

Fig. 3 SEM images of (a) Cu-BMZIFS, (b) CuCo/Zn@NPC-600 and (c) its EDS mapping.

TEM was used to further distinguish surface information of the materials. In Fig. 4a, Cu-BMZIFS shows an ordinary dodecahedron shape, which is consistent with the SEM result. As shown in Fig. 4b-d, Co metal nanoparticles are homogeneously distributed. It can be seen that the average particle size of Co nanoparticles increases with increasing the calcination temperature (Fig. S2) and this conclusion is also supported by the XRD result (Fig. 1). When the calcination temperature is elevated from 500 °C to 700 °C, no obvious metal particle agglomeration is observed and only a minor increase in particle size can be observed from 9.5 nm to 13.2 nm. The particle size of Co nanoparticles increases sharply to 73.8 nm and 137.8 nm (Fig. 4e-f and Fig. S2) when the temperature reaches 800 °C and 900 °C. In addition, the surface of the material has obvious carbon nanotube structure in Figure 4d.

To further understand the relationship between Co nanoparticles and carbon layers, we analyzed CuCo/Zn@NPC-600 using HR-TEM. As shown in Fig. 5, the interplanar fringes of metal nanoparticles are measured with a spacing of 0.205 nm, corresponding to the (111) crystal plane of fcc Co. This indicates that the crystal lattice exposed in CuCo/Zn@NPC-600 is mainly Co (111), which is in consistence with the XRD result (Fig. 1). The absence of Cu and Zn crystal lattice for the metal nanoparticle is probably due to their low content or ultrasmall size, which is confirmed by XPS and EDS analyses. Besides, the Co nanoparticle is tightly wrapped by a highly graphitized carbon layer. The spacing of carbon layer stripes is about 0.342 nm, corresponding to (002) facet of graphite carbon. Carbon nanotube information is also observed in the Fig. 5. The appearance of nanotube structure on the surface of the material is caused by the formation of Co nanoparticles that catalyze the in-situ growth of the graphite carbon layer. TEM and SEM images clearly reveal that small metal nanoparticles (average size of 11.8 nm) are embedded in the N-doped porous carbon of CuCo/Zn@NPC-600 without any agglomeration.

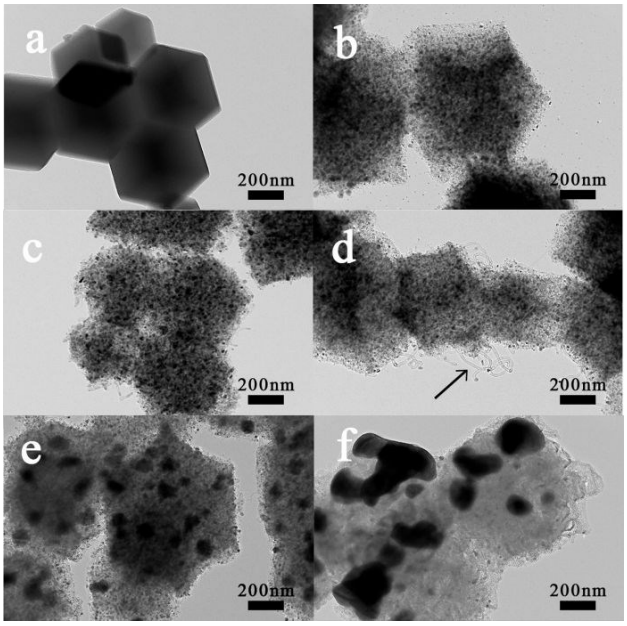

Fig. 4 TEM images of (a) Cu-BMZIFS, (b) CuCo/Zn@NPC-500, (c) CuCo/Zn@NPC-600, (d) CuCo/Zn@NPC-700, (e) CuCo/Zn@NPC-800, (f) CuCo/Zn@NPC-900.

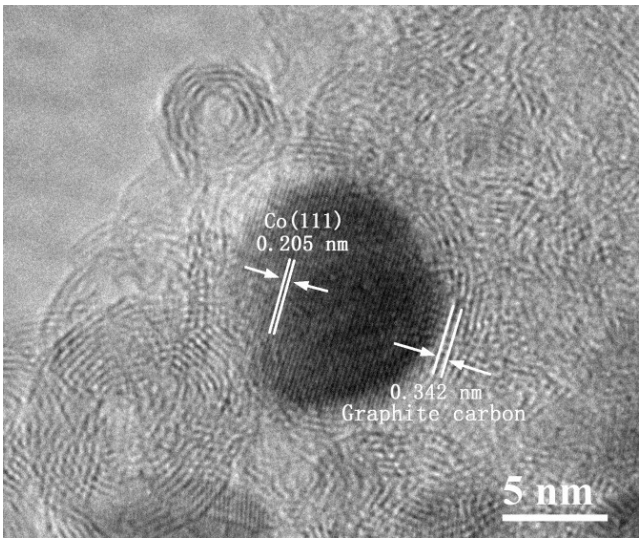

Fig. 5 HR-TEM image of the CuCo/Zn@NPC-600 material.

XPS spectra of CuCo/Zn@NPC-600 are shown in Fig. S3 and the XPS result shows that almost all elements of C, N, O, Co, Cu and Zn are present in this material (Fig. S3a). Fig. S3c shows that the XPS spectrum for N 1s exhibits four types of nitrogen species: pyridinic-N (398.4 eV), pyrrolic-N (400.4 eV), graphitic-N (401.1 eV), and oxidized-N (404.1 eV), and pyridinic-N accounts for a maximum of 70.42% (Table S1). As the pyrolysis temperature increases, pyridine-N is thermally unstable and is slowly converted to graphite-N at higher carbonization temperatures (Table S1). Furthermore, a small amount of Co-N centers may be formed during the pyrolysis of Co-based ZIF-67.[35, 41] As shown in Fig. S3e, XPS spectrum of Cu is too noisy likely due to the low Cu content, and current quality is not suitable to acquire reliable quantitative devolution of Cu components. But this observation once again proves the existence of Cu in CuCo/Zn@NPC-600. Moreover, 778.3 eV and 793.3 eV are assigned to Co(0) $2p_{3/2}$ and Co(0) $2p_{1/2}$ in the high-resolution XPS spectrum of Co 2p (Fig. S3d). CuCo/Zn@NPC-600 has the largest amount of 58.93% Co(0) (Table S1). The presence of Co^{2+} (781.0/796.2 eV) may be derived from partial oxidation of outer surface of the nanoparticle.[42] In addition, the peak of Co^{2+} $2p_{3/2}$ (781.0 eV) in CuCo/Zn@NPC-600 is 0.7 eV higher than Co^{2+} $2p_{3/2}$ (780.3 eV) in Co/Zn@NPC-600 (Fig. 6), indicating that the addition of Cu leads to the peak shift of Co^{2+} $2p_{3/2}$ from 780.3 eV to 781.0 eV. This change may be due to the interaction between Cu and Co,[43] which can cause a significant increase in the proportion of Co metal in CuCo/Zn@NPC-600. Compared with 32.27% Co in Co/Zn@NPC-600, Co metal percentage in CuCo/Zn@NPC-600 is significantly increased to 58.93% by the introduction of Cu (Table S1). We believe that the active center could be Co(0). In addition, the XPS element analysis of different samples is shown in Table S2. According to the XPS analysis, metal surface composition decreases with increasing carbonization temperature in Table S2.

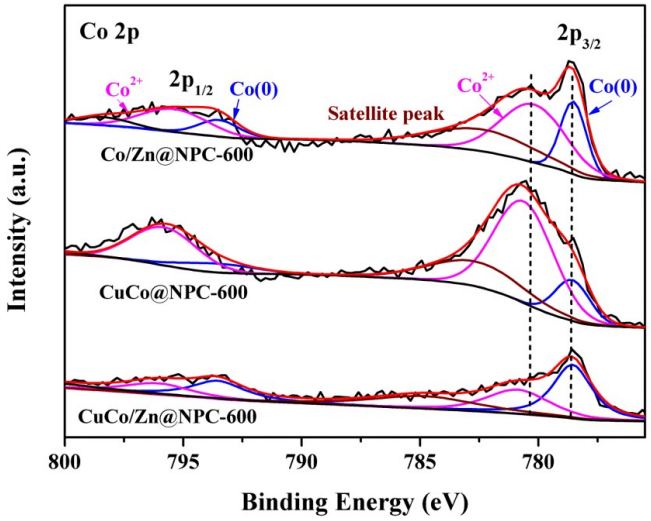

Fig. 6 XPS spectra of Co 2p for Co/Zn@NPC-600, CuCo@NPC-600 and CuCo/Zn@NPC-600 materials.

3.2 Catalytic activity

Catalytic properties of MOFs-derived catalysts with different metal components were studied. No activity is found in the hydrogenation of FF, if no catalyst or only Cu-BMZIFS precursor is added in the reactor (Table 2, Entry 1 and 2), suggesting that ionic Cu, Zn and Co species are not active centers. When single-metal catalysts of Zn@NPC-600, Cu@NPC-600 and Co@NPC-600 are used for the hydrogenation of FF under this condition, only Co@NPC-600 has a 3.3% conversion and 54.5% selectivity (Entry 3-5), shedding light on the catalytic role of Co metal. This is also proven by the bimetallic material of Cu/Zn@NPC-600 without any cobalt (Entry 6). Although Co@NPC-600 contains part of Co-N active center, due to its low conversion and selectivity, we believe that it is not dominant in catalytic hydrogenation. When Zn is added into Co@NPC-600, the conversion is remarkably increased about 14 times from 3.3% to 47.1% for

Co/Zn@NPC-600 and the selectivity is increased from 54.5% to 93.2% as well (Entry 5

Table 2 Hydrogenation of FF to FAL over different catalysts[a]

Entry	catalysts	Conversion (%)	Selectivity (%)
1	Blank	0	0
2	Cu-BMZIFS	0	0
3	Zn@NPC-600	0	0
4	Cu@NPC-600	0	0
5	Co@NPC-600	3.3	54.5
6	Cu/Zn@NPC-600	0	0
7	Co/Zn@NPC-600	47.1	93.2
8	CuCo@NPC-600	4.6	58.4
9	CuCo/Zn@NPC-600	>99.9	100
10[b]	CuCo/Zn@NPC-500	20.9	98.6
11[b]	CuCo/Zn@NPC-600	61.7	100
11[c]	CuCo/Zn@NPC-600	>99.9	100
12[c]	CuCo/Zn@NPC-700	20.7	97.5
13[c]	CuCo/Zn@NPC-800	14.8	95.9
14[c]	CuCo/Zn@NPC-900	5.4	95.1
15[b]	I-CuCo/Zn@NPC-600	40.1	96.9
16[b]	A-CuCo/Zn@NPC-600	28.9	98.1
17	Pt/C (10%)	20.3	71.2
18	Pd/C (5%)	65.6	50.4

[a] Reaction conditions: FF: 2.5 mmol; catalyst: 25 mg; THF: 8 mL; 2 MPa H_2, 140 °C, 4 h. [b] Reaction conditions: FF: 2.5 mmol; catalyst: 25 mg; THF: 8 mL; 2 MPa H_2, 130 °C, 4 h. [c] Reaction conditions: FF: 2.5 mmol; catalyst: 25 mg; THF: 8 mL; 2 MPa H_2, 170 °C, 6 h.

and 7). This simultaneous increase can be resulted from the increased porosity of Co/Zn@NPC-600 in comparison to that of Co@NPC-600, due to the fact that zinc evaporation can generate additional space at high temperature. This extra space favors contributions of more Co exposure and easy release of hydrogenated products. When a third metal Cu is introduced into CuCo/Zn@NPC-600, we can find that the conversion of above 99.9% is obtained, which is double of that for Co/Zn@NPC-600 (Entry 7 and 9). This can be interpreted by the unique porous nature, namely the big surface area of 275 m^2 g^{-1} of CuCo/Zn@NPC-600 (Table 1) provides more metal active sites and the widely distributed mesopores are more favorable for mass transport of reactants and products.[35] The result from XPS (Fig. 6) show that the introduction of Cu in CuCo/Zn@NPC-600 can alter the chemical state of Cu and Co, which can result in higher catalytic activity (Entry 7 and 9). The enhancements in both conversion and selectivity indicate the synergistic effect between Co and Cu in catalyzing FF to FAL. This hypothesis is supported by the control experiments of Co@NPC-600 and CuCo@NPC-600 (Entry 5 and 8). Moreover, I-CuCo/Zn@NPC-600 (Cu load is 1.89%) and A-CuCo/Zn@NPC-600 (Cu load is 1.28%) obtained by impregnation and adsorption show lower catalytic activity (Entry 15 and 16) compared with CuCo/Zn@NPC-600 (Entry 11), which indicated the advantage of preparation of CuCo/Zn@NPC-600 by homogeneous doping. Precious metal catalysts of Pd/C and Pt/C show lower conversion and selectivity than CuCo/Zn@NPC-600 under the same conditions (Entry 17 and 18). In addition, compared with the catalysts reported in the previous literature (Table S3), CuCo/Zn@NPC-600 has higher catalytic activity under relatively mild conditions. Therefore, the high conversion and selectivity of CuCo/Zn@NPC-600 is not only due to the addition of Zn which leads to the higher dispersed metal nanoparticles and more porous structure, but also is related to the synergism of Cu and Co.

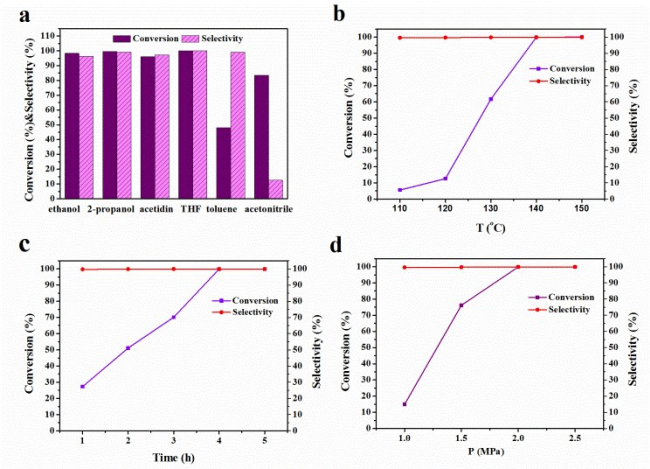

Fig. 7 (a) Effect of different solvents on conversion and selectivity for hydrogenation of FF (reaction conditions: 2.5 mmol FF, 25 mg catalyst, 2 MPa H_2, 140 °C, 4 h). (b) Effect of different reaction temperature on conversion and selectivity for hydrogenation of FF (reaction conditions: 2.5 mmol FF, 25 mg catalyst, 8 mL THF, 2 MPa H_2, 4 h). (c) Effect of different reaction time on conversion and selectivity for hydrogenation of FF (reaction conditions: 2.5 mmol FF, 25 mg catalyst, 8 mL THF, 2 MPa H_2, 140 °C. (d) Effect of different H_2 pressure on conversion and selectivity for hydrogenation of FF (reaction conditions: 2.5 mmol FF, 25 mg catalyst, 8 mL THF, 140 °C, 4 h).

N_2 adsorption and TEM characterization showed that precursor pyrolysis plays an important role on physicochemical properties of the final materials, thus the effect of pyrolysis temperature of the precursor on the catalysis performance was studied. The CuCo/Zn@NPC-T materials were explored as catalysts in the hydrogenation of FF and the results are shown in Table 2. In order to distinguish catalytic capability of CuCo/Zn@NPC-T, we adopted the catalytic reaction at 130 °C and 170 °C because the conversions of some catalysts are almost zero at 130 °C (Table 2, Entry 12-14). Obviously, CuCo/Zn@NPC-500 has a low conversion rate (20.9%) compared to CuCo/Zn@NPC-600 with a 60% conversion at 130 °C Entry 10-11). The significantly lower conversion can be ascribed to the small pores in CuCo/Zn@NPC-500 (5.7 nm) which are detrimental to facilitate the transfer of reactants and products (pore size of 6.7 nm of CuCo/Zn@NPC-600). CuCo/Zn@NPC-700 has a conversion of 20.7% (Entry 12), which is much lower than that for CuCo/Zn@NPC-600 (99.9%) in 170 °C. With elevating the pyrolysis temperature, metal particles are prone to become large by sintering or agglomeration, resulted in less available metal active sites for

catalysis. This can be supported by the larger particle size of 13.2 nm in CuCo/Zn@NPC-700 than 11.8 nm in CuCo/Zn@NPC-600. This phenomenon becomes more obvious when the temperature goes up to 800 °C or 900 °C, which can be clearly seen from the low conversions of 14.8% for CuCo/Zn@NPC-800 (73.8 nm particles) and 5.4% for CuCo/Zn@NPC-900 (137.8 nm particles) (Entry 13 and 14). In addition, it is obvious that CuCo/Zn@NPC-600 has the highest activity for catalysts carbonized at different temperatures, which is also due to the highest content of Co(0) in the metal active site (Table S1).

Solvent may play another role in liquid based heterogeneous catalysis. Herein, the effect of solvent on FF hydrogenation was investigated in Figure 7a. Toluene and acetonitrile give lower conversion and selectivity, which is probably caused by their poor hydrogen solubility.[25] The solvent for the alcohols, acetidin and THF have higher conversion and selectivity, which may be that the lone pair electron on the oxygen of solvent can form a coordination compound with the empty orbital of the metal to increase dispersing of catalyst in the system.[44-46] But THF was an optimal solvent, which gives >99.9% conversion and 100% selectivity of FAL. As shown in Fig. 7b, the reaction temperature was investigated from 110 to 150 °C over CuCo/Zn@NPC-600 catalyst. Only 5.6% and 12.6% conversion of FF was obtained at 110 °C and 120 °C. As the reaction temperature increases, FF conversion rate jumps to 61.7% at 130 °C. When the temperature reaches 140 °C, the conversion and selectivity of FF were 99.9% and 100%, respectively. It can be concluded that reaction temperature has an important effect on FF hydrogenation. It is noteworthy that FAL is the only detectable product under high temperature and THFA is not detected. This also indicates that CuCo/Zn@NPC-600 has a high selectivity for FF to FAL.

Table 3 CTH of FF over the CuCo/Zn@NPC-600 catalyst[a]

Entry	T (°C)	Time (h)	Conversion (%)	Selectivity (%)
1	100	6	45.5	100
2	110	6	54.2	99.8
3	120	6	64.9	99.6
4	130	6	91.4	99.1
5	140	6	97.3	95.3
6	130	3	73.1	99.2
7	130	4	79.8	99.3
8	130	5	85.7	99.2
9	130	7	95.8	99.1

[a]Reaction conditions: catalyst: 50 mg; FF: 1 mmol; 2-propanol: 4 mL.

The reaction time and H_2 pressure are also discussed in Fig. 7c-d. When the reaction time was elevated from 1 to 4 h, the FF conversion rate increased from 27.1% to 99.9% and selectivity remained at 99.9% with a reaction temperature of 140 °C. When the reaction time reached 5 h, the selectivity is 99.9%, which is not reduced compared to 4 h. It tells us that the reaction time was extended without the occurrence of secondary reactions leading to a decrease in selectivity during the FF hydrogenation process. The effect of H_2 pressure was surveyed by varying in the range of 1-2.5 MPa in Figure 7d. As the H_2 pressure increases from 1 MPa to 2 MPa, FF conversion increased from 14.9% to 99.9%. Obviously, the FF conversion increases with an increase of H_2 pressure. This is because the higher H_2 pressure and the greater concentration of H_2 dissolved in the solution, which is conducive to the adsorption and dissociation of H_2 on the catalyst and thus speed up the reaction. The 100% FAL selectivity of the CuCo/Zn@NPC-600 catalyst is benefited from selective hydrogenation for C=O rather than C=C bond.

In addition to H_2 as H-donor, the best catalyst of CuCo/Zn@NPC-600 was explored for CTH of FF to FAL using 2-propanol as H-donor since alcohols is more environmentally benign than pressurized H_2.[47-48] The effects of reaction time and temperature were researched for FF to FAL in CTH in Table 3. The reaction temperature is an important factor for hydrogenation of FF. When the reaction temperature goes from 100 to 130 °C, FF conversion notably increases from 45.5% to 91.4%, and >99% selectivity is obtained (Table 3, Entry 1-4). When the temperature reaches 140 °C, FF conversion increases to 97.3%, but the selectivity is slightly down to 95.3% (Entry 5). As the reaction time increases from 3 to 7 h at 130 °C (Entry 6-9), the selectivity of >99% is kept and the conversion of FF increases to 95.8% for 7 h. This result shows that the CuCo/Zn@NPC-600 catalyst is also efficient in converting FF to FAL in CTH using 2-propanol as H-donor. As shown in Table S3, the CuCo/Zn@NPC-600 catalyst has superior performance than other catalysts in CTH for FF hydrogenation.

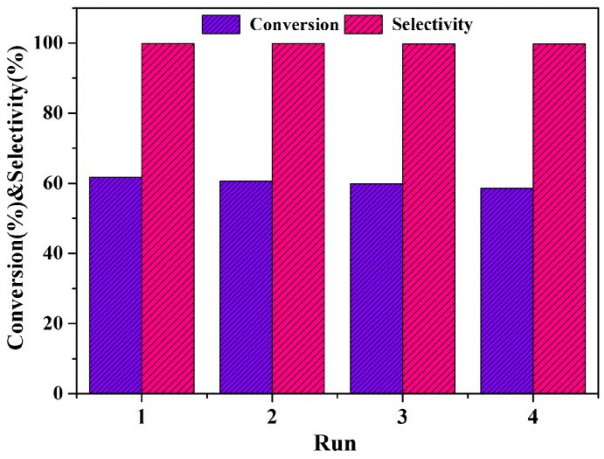

Fig. 8 Reusability of the CuCo/Zn@NPC-600 catalyst for the hydrogenation of FF. Reaction conditions: 2.5 mmol FF, 25 mg catalyst, 8 mL THF, 2 MPa H_2, 130 °C, 4 h.

After high temperature reduction, the CuCo/Zn@NPC-600 catalyst was used in cycle test. Under the same reaction conditions, the CuCo/Zn@NPC-600 could be reused at least four times, and the conversion of FF and the selectivity of FAL do not decrease significantly in Fig. 8, showing that the CuCo/Zn@NPC-600 catalyst is stable and recyclable in the conversion of FF to FAL. Fig. S5, S6 and S7 show XRD patterns, XPS spectra and TEM images of the fresh and used

CuCo/Zn@NPC-600 catalysts, which provide clues on the stability of the CuCo/Zn@NPC-600 catalyst. The XRD patterns (Fig. S5) of the used catalyst are similar to the freshly prepared catalyst. The used CuCo/Zn@NPC-600 catalyst has similar XPS spectra of Co 2p and Cu 2p (Fig. S6), indicate of maintained basic chemical state. As displayed in Fig. S7, high dispersion of the used catalysts is observed in the TEM image and there is no significant change in particle size. The activity of CuCo/Zn@NPC-600 remains unchanged in recycling experiments, which is attributed to effective inhibition of particle aggregation by N-doped porous carbon. All these evidences show that the CuCo/Zn@NPC-600 catalyst has an excellent stability. In addition, the stability of the metal is further verified by leaching test. After 2h of reaction, the catalyst is collected to exam whether the reaction could be continued. In Fig S8, the reaction conversion with the solution is 24.2% and stopped after filtering the catalyst. Comparing to the controlled experiment without filtered catalyst, the conversion rate increased almost linearly. The content of Co, Cu and Zn in filtrate doesn't reach the limit of ICP-OES after the reaction and the metal composition of the used catalysts remained almost unchanged, indicating that metal leaching has not occurred and the reaction is heterogeneous.

4. Conclusions

In summary, with Cu-BMZIFS as the precursor, the polymetallic catalyst (CuCo/Zn@NPC-600) was prepared using a facile method and applied to selective hydrogenation of FF to FAL. The hydrogenation results revealed not only >99.9% yield with H_2, but also 94.9% yield by CTH using 2-propanol as H-donor. The influencing factors were investigated in detail for the hydrogenation of FF to FAL. The analysis showed that Cu and Zn dopants significantly improved catalytic activity and the N-doped porous carbon improved the stability of the metal active center. Moreover, the CuCo/Zn@NPC-600 catalyst showed excellent stability and reusability for up to five times without significant decrease in reactivity. Such results were attributed to the highly dispersed metal nanoparticles, the advanced porous structure and the synergistic effect between Cu and Co in CuCo/Zn@NPC-600. The strategy of homogeneous doping and self-templating reported herein provides a way to get efficient and stable catalysts for hydrogenation of biomass-based compounds. However, due to the inherent complexity of the polymetallic structure, the study of its structure-activity relationship is still in its infancy, which requires further theoretical and experimental methods in the design, synthesis and catalytic performance regulation of polymetallic catalysts in the near future.

Conflicts of interest

The authors declare no conflict of interest.

Acknowledgements

This work was supported by the National Natural Science Foundation of China (No.31760190, 21531003, 21501024, 21971035), Special project of agricultural basic research in Yunnan (No.2017FG001026, 2017FG001055), Jilin Scientific and Technological Development Program (20170101198JC, 20190103017JH), Jilin Education Office (JJKH20180015KJ).

References

1 M. Besson, P. Gallezot and C. Pinel, *Chem. Rev*., 2014, **114**, 1827-1870.
2 X. Kong, R. Zheng, Y. Zhu, G. Ding, Y. Zhu and Y. Li, *Green Chem*., 2015, **17**, 2504-2514.
3 P. Zhou, Z. Zhang, L. Jiang, C. Yu, K. Lv, J. Sun and S. Wang, *Appl. Catal. B: Environ*., 2017, **210**, 522-532.
4 M. Sankar, N. Dimitratos, P. J. Miedziak, P. P. Wells, C. J. Kiely and G. J.Hutchings, *Chem. Soc. Rev*., 2012, **41**, 8099-8139.
5 S. Dutta, S. De, B. Saha and M. I. Alam, *Catal. Sci. Technol*., 2012, **2**, 2025-2036.
6 K. Yan, G. Wu, T. Lafleur and C. Jarvis, *Renew Sust. Energ Rev.*, 2014, **38**, 663-676.
7 X. Hu, R. J. M. Westerhof, D. Dong, L. Wu and C.-Z. Li, *ACS Sustain Chem. Eng*., 2014, **2**, 2562-2575.
8 R. Mariscal López and M. O. P. Maireles-Torres, I. Sadaba and M. López Granados, *Energy Environ. Sci.,*2016, **9**, 1144-1189.
9 M. J. Taylor, L. J. Durndell, M. A. Isaacs, C. M. A. Parlett, K. Wilson, A. F. Lee and G. Kyriakou, *Appl. Catal. B: Environ*., 2016, **180**, 580-585.
10 N. S. Biradar, A. M. Hengne, S. N. Birajdar, P. S. Niphadkar, P. N. Joshi and C. V. Rode, *ACS Sustain Chem. Eng*., 2014, **2**, 272-281.
11 S. Sitthisa, W. An and D. E. Resasco, *J. Catal*., 2011, **284**, 90-101.
12 T. Ishida, K. Kume, K. Kinjo, T. Honma, K. Nakada, H. Ohashi, T. Yokoyama, A. Hamasaki, H. Murayama, Y. Izawa, M. Utsunomiya, M. Tokunaga, *ChemSusChem.,* 2016, 9, 3441–3447.
13 Y. Yang, Z. Du,Y. Huang, F.Wang J. Gao and J. Xu, *Green Chem*., 2013,**15**, 1932-1940.
14 X. Li, J. Deng, T.Pan, C. Yu, H. Xu and Y. Fu, *Green Chem.*, 2015,**17**, 1038-1046.
15 J. Lange, W. D. van de Graaf and R. J. Haan, *ChemSusChem.,* 2009, **2**, 437-441.
16 S. M. Rogers, C. R. A. Catlow, C. E. Chan-Thaw, A. Chutia, N. Jian, R. E. Palmer, M. Perdjon, A. Thetford, N. Dimitratos, A. Villa and P. P. Wells, *ACS Catal.,* 2017, **7**, 2266-2274.
17 P. Gallezot, *Chem. Soc. Rev*., 2012, **41**, 1538-1558.
18 A. D. R. Rao, R. T. K. Baker and M. A. Vannice, *J. Catal*., 1997, **171**, 406−419.
19 K. Yan, C. Jarvis, T. Lafleur, Y. Qiao and X. Xie, *RSC Adv*.,2013, **3**, 25865–25871.
20 T. W. Goh, C. K. Tsung and W. Huang, *ACS Appl. Mater. Interfaces*., 2019, **11**, 23254-23260.
21 Q. Yuan, D. Zhang, L. v. Haandel, F. Ye, T. Xue, E. J. M. Hensen and Y. Guan, *J Mol Catal A-Chem.,* 2015, **406**, 58-64.
22 Y. Nakagawa and K. Tomishige, *Catal. Commun.,* 2010, **12**, 154-156.
23 S. Huang, N. Yang,S. Wang and Y. Zhu, *Nanoscale*., 2016, **8**, 14104-14108.
24 S. Bhogeswararao and D. Srinivas, *J. Catal.*, 2015, **327**, 65-77.
25 W. Gong, C. Chen, Y. Zhang, H. Zhou, H. Wang, H. Zhang, Y. Zhang, G. Wang and H. Zhao, *ACS Sustain Chem. Eng*., 2017, **5**, 2172-2180.
26 M. Audemar, C. Ciotonea, K. De Oliveira Vigier, S. Royer, A. Ungureanu, B. Dragoi, E. Dumitriu and F. Jérôme, *ChemSusChem*, 2015, **8**, 1885-1891.
27 T. Mitsudome and K. Kaneda, *Green Chem.,* 2013, **15**, 2636-2654.

View Article Online
DOI: 10.1039/D0NR04098C

28 Y. Dong and F. Zaera, *J. Phys. Chem. Lett.,* 2018, **9**, 1301-1306.
29 X. Liu, Eileen H. Yu and K. Scott, *Appl. Catal. B: Environ*., 2015, **162**, 593-601.
30 Y. Feng, G. Yan, T. Wang, W. Jia, X. Zeng, J. Sperry, Y. Sun, X. Tang, T. Lei and L. Lin, *Green Chem.,* 2019, **21**, 4319-4323.
31 G. Gumilar, Y. V. Kaneti, J. Henzie, S. Chatterjee, J. Na, B. Yuliarto, N. Nugraha, A. Patah, A. Bhaumik and Y. Yamauchi, *Chem. Sci.,* 2020, **11**, 3644-3655.
32 Y. V. Kaneti, S. Dutta, M. S. A. Hossain, M. J. A. Shiddiky, K. L. Tung, F. K. Shieh, C. K. Tsung, K. C. Wu and Y. Yamauchi, *Adv. Mater.,* 2017, **29**, 1700213.
33 S. R. Venna, J. B. Jasinski and M. A. Carreon, *J. Am. Chem. Soc.*, 2010, **132**, 18030-18033.
34 R. Banerjee, A. Phan, B. Wang, C. Knobler, H. Furukawa, M. O'Keeffe and O. M. Yaghi, *Science.*, 2008, **319**, 939-943.
35 Y. Z. Chen, C. Wang, Z. Y. Wu, Y. Xiong, Q. Xu, S. H. Yu and H. L. Jiang, *Adv. Mater.*, 2015, **27**, 5010-5016.
36 C. Wang, J. Kim, J. Tang, M. Kim, H. Lim, V. Malgras, J. You, Q. Xu, J. Li and Y. Yamauchi, *Chem.,* 2020, **6**, 19-40.
37 Y. Shi, Y. Zhu, Y. Yang, Y.-W. Li and H. Jiao, *ACS Catal.,* 2015, **5**, 4020-4032.
38 S. Sitthisa, T. Sooknoi, Y. Ma, P. B. Balbuena and D. E. Resasco, *J. Catal.*, 2011, **277**, 1-13.
39 A. Phan, C. J. Doonan, F. J. Uribe-Romo, C. B. Knobler, M. O'Keeffe and O. M. Yaghi, *Acc. Chem. Res.,* 2010, **43**, 58-67.
40 H. Yang, X.-W. He, F. Wang, Y. Kang and J. Zhang, *J. Mater. Chem.,* 2012, **22**, 21849-21851.
41 X. Wang and Y. Li, *J Mol Catal A-Chem.,* 2016, **420**, 56-65.
42 Y. Zhou, Y. Chen, L. Cao, J. Lu and H. Jiang, *Chem. Commun.,* 2015, **51**, 8292-8295.
43 W. Guo, H. Liu, S. Zhang, H. Han, H. Liu, T. Jiang, B. Han and T. Wu, *Green Chem.,* 2016, **18**, 6222-6228.
44 X.Y. Wang and R. Rinaldi, *ChemSusChem.,* 2012,**5**, 1455-1466.
45 I. McManus, H. Daly, J.M. Thompson, E. Connor, C. Hardacre, S.K. Wilkinson, N.Sedaie Bonab, J. ten. Dam, M.J.H. Simmons, E.H. Stitt, C. D'Agostino, J.McGregor, L.F. Gladden and J.J. Delgado, *J. Catal.,* 2015, **330**, 344-353.
46 J. Wu, G. Gao, J. Li, P. Sun, X. Long and F. Li, *Appl. Catal. B: Environ*., 2017, **203**, 227-236.
47 P. Panagiotopoulou and D. G. Vlachos, *Appl. Catal.A, Gen*., 2014, **480**, 17-24.
48 J. Du, J. Zhang, Y. Sun, W. Jia, Z. Si, H. Gao, X. Tang, X. Zeng, T. Lei, S. Liu and L. Lin, *J. Catal.*, 2018, **368**, 69-78.

View Article Online
DOI: 10.1039/D0NR04098C

Graphical Abstract:

Tuning the synthesis of polymetallic-doped ZIFs derived materials for efficient hydrogenation of furfural to furfuryl alcohol

Yafei Fan,[a] Shangjing Li,[a] Ying Wang,[a] Changfu Zhuang,*[a] Xiaoteng Liu,[c] Guangshan Zhu[b] and Xiaoqin Zou*[b]

[a] Key Laboratory of Forest Resources Conservation and Utilization in the Southwest Mountains of China, Ministry of Education, Southwest Forestry University, Kunming 650051, P. R. China.

[b] Faculty of Chemistry, Northeast Normal University, Changchun 130024, P. R. China.

[c] Department of Mechanical and Construction Engineering, Faculty of Engineering and Environment, Northumbria University, Newcastle upon Tyne, NE1 8ST, UK.

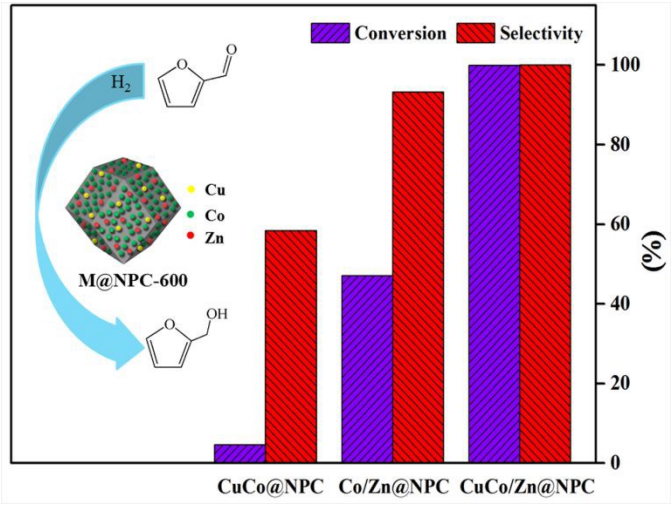

Cu, Co and Zn modified N-doped porous carbons (CuCo/Zn@NPC) are prepared using a polymetallic homogeneous doping and self-templating method as high performance non-noble metal catalysts for the selective hydrogenation of furfural to furfuryl alcohol.